Intense proton acceleration in ultrarelativistic interaction with nanochannels

L. A. Gizzi ©,[1,2,*] G. Cristoforetti ©,[1,†] F. Baffigi,[1] F. Brandi ©,[1] G. D'Arrigo ©,[3] A. Fazzi ©,[4,5] L. Fulgentini,[1] D. Giove,[5]
P. Koester,[1] L. Labate,[1,2] G. Maero ©,[6,5] D. Palla,[1] M. Romé ©,[6,5] M. Russo,[3] D. Terzani ©,[1] and P. Tomassini[1]

[1]*1 ILIL, Istituto Nazionale di Ottica, CNR, Pisa, Italy*
[2]*INFN, Sezione di Pisa, Pisa, Italy*
[3]*Istituto per la Microelettronica e Microsistemi, CNR, Catania, Italy*
[4]*Dipartimento di Energia, Politecnico di Milano, Milan, Italy*
[5]*INFN, Sezione di Milano, Milan, Italy*
[6]*Dipartimento di Fisica, Universitá degli Studi di Milano, Milan, Italy*

We show that both the flux and the cutoff energy of protons accelerated by ultraintense lasers can be simultaneously increased when using targets consisting of thin layers of bundled nanochannels. Particle-in-cell simulations suggest that the propagation of an electromagnetic field in the subwavelength channels occurs via excitation of surface plasmon polaritons that travel in the channels down to the end of the target, sustaining continuous and efficient electron acceleration and boosting acceleration of protons via enhancement of the target normal sheath acceleration mechanism.

I. INTRODUCTION

The capability of relativistic laser pulses to accelerate light ions has been intensively investigated in recent years as a way to build new compact laser-based accelerators. Among the various mechanisms, target normal sheath acceleration (TNSA) [1] has the advantage of being robust and giving rise to laminar, high-brightness ion pulses [2,3]. In the typical setup, a few-microns-thick solid foil is irradiated by an intense laser pulse and ions on the rear surface are accelerated by a sheath field produced by so-called hot electrons (HE) that are generated during the laser-plasma interaction. The accelerating sheath field E_s depends on both the number density n_h and the temperature T_h of the HE [4], where $E_s \propto \sqrt{T_h n_h}$. Higher ion cutoff energies and fluxes are therefore expected for target geometries able to increase the number and/or the temperature of the generated HE.

Recently, relativistic interaction of ultrashort laser pulses with nano- or micro-structured targets has attracted interest, mainly because of the enhanced efficiency of laser absorption. Depending on the target geometry, the improved laser-target coupling can result in a volumetric heating of the plasma up to extreme temperatures [5], in a more efficient x-ray emission [6] or in an efficient production of HE [7–9]. It was shown that for aligned arrays of micropillars or microchannels, the

*leonidaantonio.gizzi@cnr.it
†gabriele.cristoforetti@cnr.it

interaction can lead to mega-Ampere currents of relativistic electrons propagating into the target [10], resulting in the self-generation of a mega-Gauss magnetic field on its rear surface [11]. Kinetic particle-in-cell (PIC) simulations suggest that the larger HE generation is related to the enhancement of electrostatic fields [8] or to the generation of propagating electromagnetic (e.m.) waves [12] in the proximity of the nanostructures. Such phenomena can be related to analogous mechanisms known in solid-state plasmonics [13], namely the enhancement of electrostatic fields due to a localized surface plasmon resonance (SPR) and the excitation of propagating surface plasmon polaritons (SPP).

In solids, SPP can be excited by light irradiation of dielectric-metal interfaces, where an abrupt jump of the dielectric function from a positive to a negative value exists. SPP are e.m. waves strongly confined near the interface and propagating along it, often for considerable distances. They reduce to electrostatic localized SPR for high wave-vector values ($k_{\rm SPP} = \frac{2\pi}{\lambda_{\rm SPP}} \gg k_0 = \frac{2\pi}{\lambda_0}$) and to Sommerfeld-Zenneck waves [14,15], i.e., grazing confined light waves, when $k_{\rm SPP} \approx k_0$. The high confinement of the SPP fields, due to the evanescent character into both the dielectric medium and the metal bulk, allows them to propagate into plasmonic devices of dimensions beyond the diffraction limit.

In the relativistic irradiation regime [16], laser-plasma interaction is ruled by the dielectric function $\epsilon = 1 - \omega_p^2/\gamma \omega_0^2$, where ω_p and ω_0 are the plasma and the laser angular frequencies, and γ accounts for the relativistic quivering of the electron. Here, solid targets are ionized within the laser cycle and $\omega_p \gg \omega_0$ and thus $\epsilon \ll 0$, which prevents the laser light from penetrating into the plasma, beyond a skin depth of a few nanometers. We note that the above expression of the dielectric function reduces to that of a metal derived with the Drude model, when $\gamma = 1$ (nonrelativistic regime) and ω_p

is set by the valence electrons in the metal. The extension of solid-state plasmonics theory to the high-fields regime is therefore straightforward, provided that nonlinear relativistic effects of electron dynamics are accounted for [16].

In solid-state plasmonics excitation of SPP is made difficult by the phase matching between SPP and light waves, since $k_{SPP} > k_0$. In the case of flat dielectric-metal interfaces, this issue can be circumvented by using appropriate coupling configurations [13]. Excitation of SPP is, however, easier by using nanostructured surfaces, where momentum compensation is made possible by different irradiation schemes, including the grating-assisted coupling and the photon scattering at points of structural symmetry breaking [17]. In gratings, the metal surface is patterned by grooves with an appropriate periodicity, so that phase matching becomes possible for appropriate angles of laser incidence. Recently, this scheme to excite SPP has been experimentally demonstrated also in the high-field regime [18,19]. The excitation of SPP on nanowires or nanotube arrays is easier, since the structural symmetry breaking allows the phase matching. In the high-field regime, SPP could be excited by irradiating nanowire-nanotube array targets at relativistic intensity and this could explain the mega-ampere currents of HE measured in these configurations [11]. Zou *et al.* [20–22] showed via PIC simulations that relativistic laser interaction with microchannels generates propagating e.m. fields able to accelerate relativistic electrons at super-ponderomotive energies; distributed as TM eigenmodes into a waveguide, such fields have a spatial distribution similar to that expected for SPP waves. Interestingly, those simulations also show that if a CH foil is placed at the end of the microchannel, TNSA acceleration of protons to energies three times higher than plane CH targets could be observed.

In this work, we demonstrate experimentally that the irradiation of TiO$_2$ nanochannel targets at ultrarelativistic intensity efficiently accelerate protons via TNSA. Our measurements show that both proton flux and cutoff energy are significantly higher than those measured with flat titanium foils of a comparable thickness. Particle-in-cell simulations account for the formation of SPP waves traveling along the nanochannel walls, leading to an effective acceleration of energetic electrons and to a higher sheath field at the rear side of the target. The unique plasmonic character of the e.m. waves is here corroborated by the size of the channel, smaller than the diffraction limit, that inhibits the propagation of laser light.

II. EXPERIMENTAL RESULTS

The measurements were carried out at the Intense Laser Irradiation Laboratory (ILIL) using the ILIL Ti:Sa laser in a 100-TW configuration delivering 3 J on target [23]. The laser pulse ($\lambda = 800$ nm, $\tau = 30$ fs) was focused by a $f/\#4.5$ off-axis parabola (OAP) in a spot of $\approx 3 \times 5$ μm^2 (FWHM), at an angle of incidence of 15°, giving a laser intensity of $\approx 2.8 \times 10^{20}$ W/cm^2 ($a_0 \simeq 11$), corresponding to a Strehl ratio of 0.54. The target consisted of an array of closely packed 14-μm-long TiO$_2$ nanochannels [24], open on both ends, as shown in Fig. 1.

The channels have an internal diameter of ≈ 120 nm and are separated by an ≈ 50-nm-thick wall. Ion acceleration from nanochannel targets was compared to that obtained from pure
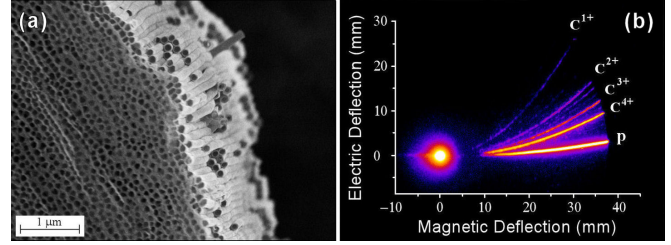

FIG. 1. (a) SEM image of a TiO$_2$ nanochannel array target. (b) Raw image obtained with the Thomson Parabola detector from a nanochannel target.

titanium foils of 12.5 μm thickness, used here as a reference target for standard TNSA. Because of the weak dependence on target thickness observed in previous measurements [25], we assume that the small difference in thickness cannot account for the observed differences in proton acceleration. Also, difference in target composition is expected to play a minor role in TNSA measurements as studied in previous systematic experiments [25]. Samples were mounted in a target holder ensuring sub-micrometer-level positioning [26].

The nanosecond ASE laser contrast was better than 10^9 while the contrast at 10 ps was better than 10^7 [26]. Accounting for the different divergence of the ASE with respect to that of the main beam [27], however, we estimate an ASE intensity on target of the order of 10^9 W/cm^2, well below the plasma formation threshold. The low value of ASE intensity also prevents a significant degradation of the nanotube target before the arrival of the main peak. The ps pedestal leads to the formation of a short scale-length preplasma a few ps before the laser peak. Dedicated hydrodynamic simulations on Ti flat targets show that the density scale length of such preplasma at the critical density is ≈ 200 nm, which is consistent with previous detailed studies [28]. The effect of the ps pedestal on TiO$_2$ nanochannels is less straightforward due to the different target geometry. However, the preplasma length in the front side is expected to be smaller than that in front of the flat target because the ablation thresholds of insulators is higher by at least an order of magnitude. Moreover, due to the size of the nanotubes, smaller than the diffraction limit, it is unlikely that a large energy fraction of the ps pedestal can penetrate into the target, except a small percentage propagating via plasmonic effects in solid nanostructures. This suggests that only an underdense preplasma can be present into the nanochannels during the main peak interaction [7,29].

Ion acceleration was investigated by means of a Thomson parabola (TP) and a time-of-flight (TOF) silicon carbide fast diode. TP and TOF were both placed behind the target, aligned on the normal direction to the surface and on a slightly tilted direction ($\approx 4°$), respectively. TP and TOF detectors, described in Ref. [26], were used simultaneously to allow a cross check of the measurements.

A typical raw TP image obtained for a nanochannel target is presented in Fig. 1 showing the trace of protons, along with carbon and oxygen ions originating from the hydrocarbon contaminants on the target rear surface [2]. The central bright spot, at the origin of the parabolas, is produced by x-ray radiation shining through the TP collimator.
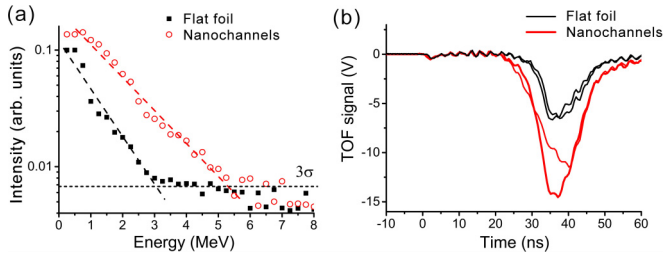
FIG. 2. (a) Single-shot proton spectra obtained for flat titanium foil (black squares) and nanochannel TiO_2 target (red circles). The horizontal dashed line represents the 3σ noise level. (b) TOF signals obtained from two shots on flat foils (black curves) and two shots on nanochannel targets (red curves).

Typical single-shot proton spectra obtained from TP data using a titanium foil and a TiO_2 nanochannel target are reported in Fig. 2(a). As shown, nanochannels provide a larger flux of protons and a higher cutoff energy. The cutoff energy for the nanochannel targets, calculated by considering a signal threshold of three times the noise rms, is in the range $(4.3–6.0) \pm 0.2$ MeV, i.e., averaging over three consecutive shots ≈1.5 times higher than the average value obtained for the Ti foil, in the range $(3.3–4.0) \pm 0.2$ MeV.

The enhancement of the cutoff energy was confirmed by the TOF measurements. Traces of the TOF signal for both Ti foils and TiO_2 nanochannels are also reported in Fig. 2, showing that, for nanochannels, protons reach the detector at earlier times. Also, the signal amplitude is ≈3 times higher than that obtained for flat foils. Here, however, due to the lower sensitivity of the TOF detector and possibly also to the off-axis viewing angle (≈4°), the measured cutoff values for foils and nanochannels are ≈2.8 MeV and ≈4.2 MeV, respectively, confirming, however, the ≈1.5 increase for nanochannel targets.

To our knowledge, the simultaneous increase of proton cutoff energy and ion flux from nanochannel targets, compared to flat foil targets, was not observed before and cannot be explained by target composition or thickness. According to our estimation of plasma expansion reported above, we do not expect that the preplasma formed in front of the nanochannel targets can result in a more efficient acceleration of hot electrons with respect to a flat target. As discussed below, our model based on SPP provides a satisfactory interpretation of our experimental observation.

III. MODELLING AND DISCUSSION

Particle-in-cell simulations were carried out with the ALaDyn code [30] in two-dimensional (2D) Cartesian geometry. The p-polarized laser pulse, with Gaussian intensity profile in the transverse coordinate and focal spot FWHM = 4 μm, enters in the computational box from the left edge [Fig. 3(a)] and impinges on the target at normal or at 15° incidence at time $ct \approx 13 \, \mu$m, i.e., ≈43 fs after the beginning of the simulation. The laser temporal profile was modelled by $I(t) = I_0\cos^4(\pi t/2\tau)$, where $2\tau = 84$ fs corresponds to a pulse length FWHM of 30 fs. The size of the numerical box was set to $L_x L_y = 80 \times 60 \, \mu$m^2 and the grid cell to $dx dy = 12 \times 6$ nm^2 with 144 (macro)electrons and 324
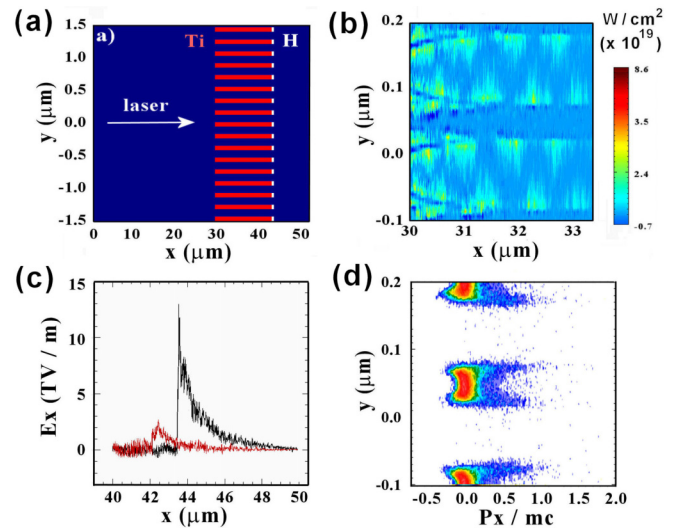

FIG. 3. (a) Portion of the simulation box showing the target model, (b) longitudinal component of the Poynting vector (W/cm^2) of the e.m. field at time $ct = 10 \, \mu$m, (c) longitudinal sheath electric field E_S near the rear side of the target for flat (red curve) and nanochannel (black curve) targets at time $ct = 30 \, \mu$m, and (d) longitudinal momentum Px vs y position at time $ct = 10 \, \mu$m. Images refer to normal laser irradiance and a nanochannel target with a gap size of 100 nm.

(macro)protons per cell. The target consisted of pure titanium in both nanochannel and foil targets simulations, with an initial Ti^{2+} density of 5.2×10^{22} cm^{-3}, corresponding to an electron density $n_e = 60 \, n_c$. Because of the 2D character of the simulation, the nanochannel target was modeled as a regular array of Ti nanowires of 50 nm, separated by gaps of different size. The relevance of this structure to the actual 3D nanochannel structure will be discussed below. A thin layer of hydrogen was placed behind the nanochannel tips rear side as a source of ions. Field ionization using the ADK model was activated, which resulted in the increase of Ti ionization level from the initial $Z = 2$ to a final $Z \approx 18$ in the nanochannel walls, during laser-plasma interaction.

The normalized energy distributions of the protons at the end of the simulation ($ct = 70 \, \mu$m), taken behind the target, are plotted in Fig. 4(a), showing a good agreement of the cutoff energies with experimental data (Fig. 2). Normal laser irradiation ($\theta = 0$) results in a higher cutoff with respect to irradiation at $\theta = 15°$. The proton spectrum obtained by irradiating a flat target at an angle $\theta = 15°$ is also reported in the figure. In this case, an exponential preplasma ramp with density scalelength of 150 nm was placed in front of the target to reproduce the expected interaction conditions. Simulations show that the increase of the cutoff energy obtained with nanochannel targets is produced by the enhancement of the sheath field E_S on the rear target surface by a factor ≈5, as shown in Fig. 3(c). For nanochannels, this field reaches values of a few tens of TV/m, depending on the gap size, compared to a few TV/m obtained for a flat target; this results in the generation of a proton beam with a small angular divergence ($\Delta\varphi < 10°$), which is emitted normally to the rear surface,
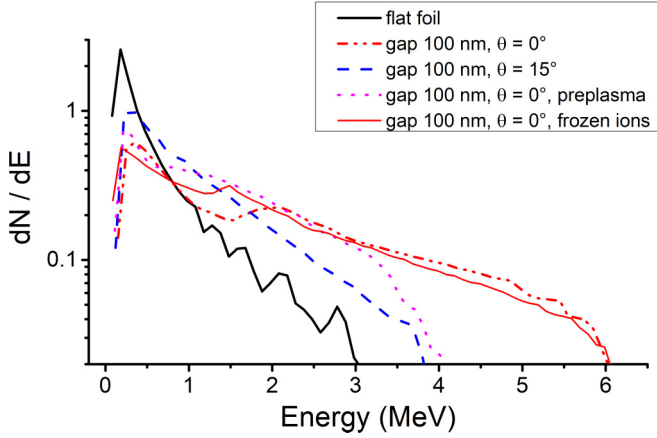
FIG. 4. Normalized spectral distributions of protons obtained by PIC simulations at time $ct = 70~\mu$m for a 100-nm gap size and with incidence angles $\theta = 0°$ and $\theta = 15°$. Spectra obtained in the case where gaps are filled by a pre-plasma with $n_e = 0.025~n_c$ and in the case where ions are frozen during the simulations are also shown. The flat foil case is shown for comparison.

whatever is the angle of laser incidence on the front target surface.

Further simulations were carried out by including a homogeneous underdense preplasma $0.02 < n_e/n_c < 1$ into the nanochannel gaps to account for the effect of the laser ps pedestal discussed above. The results show that the presence of a preplasma results in a less effective proton acceleration with lower cutoff energies due to a degradation of the laser-plasma coupling, as shown in Fig. 4 for the case of a preplasma of $n_e = 0.025~n_c$.

A deeper insight into the mechanisms leading to proton acceleration using nanochannel targets can be obtained examining the electromagnetic fields propagating into the target. At early times, i.e., when the leading part of the laser pulse hits the front surface, the interaction gives rise to e.m. fields propagating into the gaps along the edges of the channels, where electric and magnetic fields oscillate in transverse directions; in phase with this e.m. field, an oscillating longitudinal electrostatic field is also visible near the edge of the channels. The e.m. field is clearly shown in Fig. 3(b), where the Poynting vector of the e.m. waves is plotted at time $ct = 10~\mu$m in the front part of the target (nanochannel tips are located at $x = 29.5~\mu$m). The trailing part of the laser pulse, at the opposite, is largely reflected by the plasma expanding at the tips, which rapidly fills the vacuum gaps as visible on the left side of Fig. 3(b). The e.m. field has the structure of a SPP wave, moving along the nanochannel edge, which separates the underdense (gap) and the overdense (wall) plasma region with dielectric functions of opposite sign. As expected, the intensity of the e.m. field rapidly falls with an evanescent behavior for increasing distance from the nanochannel-gap interface, showing a confinement of the wave close to the wall. By considering the continuity relation of ϵE_y at the vacuum-wall interface, the transverse electric field E_y into the overdense plasma is expected to be lower than into the gap by a factor of $\approx (1 - n_{e,+}/\gamma n_c)/(1 - n_{e,-}/\gamma n_c) \approx 50$, where $n_{e,+}$ and $n_{e,-}$ are the electron densities in the wall
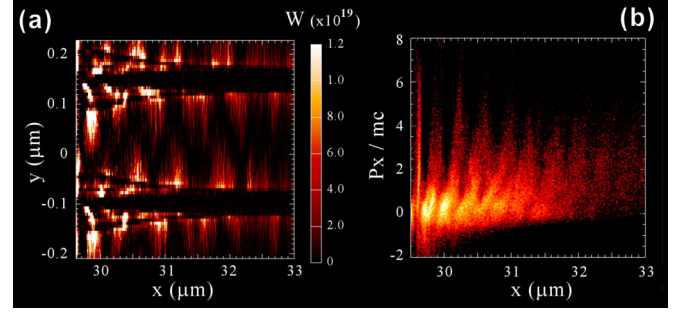

FIG. 5. (a) Longitudinal component of the Poynting vector (W/cm^2) of the e.m. field. (b) longitudinal momentum P_x vs x of electrons located into the channels. Both images refer to a nanochannel gap of 200 nm and to a simulation time $ct = 10~\mu$m.

and in the gap, respectively. The spatial distribution of the e.m. field is here significantly different from that obtained with microchannel targets [10], where the larger size allows the laser light to freely propagate into the channels. Nevertheless, the fields obtained by Zou *et al.* [20] at the edge of the channels, including e.m. and electrostatic surface waves, is similar to our results. Here, the fields exhibits the typical asymmetric zigzag distribution, which is usually produced by the interference of Transverse Magnetic TM$_0$ and Transverse Electric TE$_1$ modes [31]; a similar distribution was clearly observed in classical plasmonics by imaging the luminescence of quantum dots covering the nanowire lateral surface [32]. The asymmetric transverse structure of the fields can also be driven by the coupling of the opposite evanescent fields into the gap.

Figure 3(b) shows that the wave vector of the surface e.m. wave is $k_{SPP} \sim k_0$, as expected for cases where $\omega_0 << \omega_p$, and the SPP acquires the features of a Sommerfeld-Zenneck wave [14,15]. This makes easier the momentum matching with the laser light and therefore the SPP excitation at the nanochannel tip. Simulations also show that the increase of the nanochannel diameter leads to a better laser-SPP coupling, resulting in higher energy transferred to the surface wave. For a diameter of 100 nm, the Poynting vector of the SPP is only $\approx 9\%$ of that of the incident laser, but it rises to $\approx 15\%$ and $\approx 30\%$ for diameters of 150 and 200 nm. This leads to higher proton cutoff energies when larger nanochannels are used, rising from ≈ 6.4 MeV for a 100-nm gap to ≈ 7.3 MeV and ≈ 7.7 MeV for diameters of 150 and 200 nm, respectively.

The inspection of the electron phase space P_x versus y plot of Fig. 3(d) shows that the SPP fields produce the electron acceleration into the nanochannels via the $\vec{J} \times \vec{B}$ force and by the longitudinal electrostatic field, occurring mainly at the wall-gap interface. The phase space P_x versus x plot of the electrons contained in the gap [Fig. 5(b)] shows that the most energetic electrons are spatially bunched at the positions where the SPP fields are peaked. This is evident by comparing the spatial modulation of the Poynting vectors and of the electron bunching for a nanochannel of 200 nm, shown in Fig. 5.

The spatial bunching of the electrons into the channels show that electrons, initially extracted from the overdense region, gain energy from the SPP wave, damping its further

propagation. The backward motion of thermal bulk electrons into the wall provides a return current neutralizing charge separation and allows the forward acceleration of HE.

Particular attention was also deserved to the effects produced by the plasma filling of the channels on electron acceleration. Here, we focus on the wire expansion during the interaction of the main laser peak and not on the preplasma generated by the laser pedestal. PIC simulations show that the channels are filled at the relativistic critical density γn_c at a late time of interaction, i.e., around 12 fs after that the laser peak impinges on the target surface. Results also show that SPP are efficiently excited until that time, i.e., until the density into the channels is $\approx \gamma n_c$. In order to investigate the effect of channel filling, we carried out PIC simulations in the same conditions as before but with the ions kept frozen. In this case, the excitation of SPP waves into the channels was still clearly observed, but the gaps were not filled by wire expansion, so that the nanochannel array structure remained intact during the whole pulse duration. As shown in Fig. 4, the energy cutoff of the accelerated protons obtained in simulations with frozen ions is the same as that obtained in simulations with moving ions. This clearly shows that the electron acceleration by the SPP fields is largely dominant over the electron acceleration due to the interaction with the plasma eventually filling the gaps.

As for the extrapolation of the above PIC simulations to the 3D geometry, this aspect was discussed elsewhere and 2D simulations were found to satisfactorily address interaction and absorption effects [33,34], provided the modeled 2D structure is representative of the experiment. Here, as discussed above, the target model represented in Fig. 3(a) is the projection on the polarization plane of both nanowire and nanochannel targets which, in principle, are expected to produce different behaviors. The wide literature in solid-state plasmonics can be, however, a reference source to try to extend our results in the 3D geometry. In nanochannels, finite-difference-time-domain simulations and experiments show a strong dependence of SPR wavelength and SPP modes on the size and the thickness of the gaps and on the composition of the medium in which nanochannels are embedded [35,36]. Similarly to nanowires, SPP waves with different azimuthal symmetry ($m = 0 \pm 1, \pm 2, ...$) can be excited on

the dielectric-metal interface [35,37,38]. Such modes can be excited in the dielectric medium both inside and outside the tube. In the present case, due to the array structure, only the former modes can be excited. The parallelism with solid-state plasmonics suggests that the formation of SPP modes obtained by our 2D PIC simulations could be extrapolated to 3D geometry, which should, however, be verified in future work. We also stress that, in general, 2D simulations tend to overestimate the cutoff energy of the proton spectrum. In fact, 2D simulations exhibit a logarithmic growth of the cutoff energy with time, and therefore, the cutoff energy depends upon an arbitrary choice of the end of the simulation [39]. Consequently, 2D simulations are mainly used here for a qualitative comparison between the foil and the nanostructured targets, with the end of simulation corresponding approximately to the time at which the simulated cutoff proton energy matches the experimental value for flat foil measurements.

IV. CONCLUSIONS

In summary, we found that nanochannel targets can significantly enhance the TNSA laser-driven proton acceleration via excitation of surface plasmon polaritons. In our experiment, a 3 times higher flux and a 1.5 times enhancement of the energy cutoff was found with respect to flat foils. PIC simulations suggest that, similarly to solid-state plasmonics, the propagation of e.m. fields in nanochannels with a subwavelength size is made possible by the excitation of surface plasmon polaritons at the interface between vacuum (hole) and overdense (wall) plasma. While being damped by the acceleration of the electrons, SPP efficiently propagate at the speed of light up to the end of the channels, assuring a continuous acceleration of the electrons. Simulations finally indicate that the efficiency of this mechanism can be further improved by increasing the size of the holes.

[1] S. C. Wilks, A. B. Langdon, T. E. Cowan, M. Roth, M. Singh, S. Hatchett, M. H. Key, D. Pennington, A. MacKinnon, and R. A. Snavely, Phys. Plasmas **8**, 542 (2001).

[2] A. Macchi, M. Borghesi, and M. Passoni, Rev. Mod. Phys. **85**, 751 (2013).

[3] H. Daido, M. Nishiuchi, and A. S. Pirozhkov, Rep. Prog. Phys. **75**, 056401 (2012).

[4] S. P. Hatchett, C. G. Brown, T. E. Cowan, E. A. Henry, J. S. Johnson, M. H. Key, J. A. Koch, A. B. Langdon, B. F. Lasinski, R. W. Lee, A. J. Mackinnon, D. M. Pennington, M. D. Perry, T. W. Phillips, M. Roth, T. C. Sangster, M. S. Singh, R. A. Snavely, M. A. Stoyer, S. C. Wilks, and K. Yasuikec, Phys. Plasmas **7**, 2076 (2000).

[5] M. A. Purvis, V. N. Shlyaptsev, R. Hollinger, C. Bargsten, A. P. A. Prieto, Y. Wang, B. M. Luther, L. Yin, S. Wang, and J. J. Rocca, Nat. Photonics **7**, 796 (2013).

[6] R. Hollinger, C. Bargsten, V. N. Shlyaptsev, V. Kaymak, A. Pukhov, M. G. Capeluto, S. Wang, A. Rockwood, Y. Wang, A. Townsend, A. Prieto, P. Stockton, A. Curtis, and J. J. Rocca, Optica **4**, 1344 (2017).

[7] G. Cristoforetti, P. Londrillo, P. K. Singh, F. Baffigi, G. D'Arrigo, A. D. Lad, R. G. Milazzo, A. Adak, M. Shaikh, D. Sarkar, G. Chatterjee, J. Jha, M. Krishnamurthy, G. R. Kumar, and L. A. Gizzi, Sci. Rep. **7**, 1479 (2017).

[8] D. Sarkar, P. K. Singh, G. Cristoforetti, A. Adak, G. Chatterjee, M. Shaikh, A. D. Lad, P. Londrillo, G. D'Arrigo, J. Jha, M.

Krishnamurthy, L. A. Gizzi, and G. R. Kumar, APL Photon. **2**, 066105 (2017).

[9] A. Moreau, R. Hollinger, C. Calvi, S. Wang, Y. Wang, M. G. Capeluto, A. Rockwood, A. Curtis, S. Kasdorf, V. N. Shlyaptsev, V. Kaymak, A. Pukhov, and J. J. Rocca, Plasma Phys. Control. Fusion **62**, 014013 (2020).

[10] J. Snyder, L. Ji, K. George, C. Willis, G. Cochran, R. Daskalova, A. Handler, T. Rubin, P. Poole, D. Nasir, A. Zingale, E. Chowdhury, B. Shen, and D. Schumacher, Phys. Plasmas **26**, 033110 (2019).

[11] G. Chatterjee, P. K. Singh, S. Ahmed, A. P. L. Robinson, A. D. Lad, S. Mondal, V. Narayanan, I. Srivastava, N. Koratkar, J. Pasley, A. K. Sood, and G. R. Kumar, Phys. Rev. Lett. **108**, 235005 (2012).

[12] A. Andreev, K. Platonov, J. Braenzel, A. Lubcke, S. Das, H. Messaoudi, R. Grunwald, C. Gray, E. McGlynn, and M. Schnurer, Plasma Phys. Control. Fusion **58**, 014038 (2016).

[13] S. A. Maier, *Plasmonics: Fundamentals and Applications* (Springer Science and Business Media, Berlin, 2007).

[14] J. Zenneck, Ann. Phys. **328**, 846 (1907).

[15] A. Sommerfeld, Ann. Phys. **333**, 665 (1909).

[16] A. Macchi, Phys. Plasmas **25**, 031906 (2018).

[17] H. Wei, D. Pan, S. Zhang, Z. Li, Q. Li, N. Liu, W. Wang, and H. Xu, Chem. Rev. **118**, 2882 (2018).

[18] T. Ceccotti, V. Floquet, A. Sgattoni, A. Bigongiari, O. Klimo, M. Raynaud, C. Riconda, A. Heron, F. Baffigi, L. Labate, L. A. Gizzi, L. Vassura, J. Fuchs, M. Passoni, M. Kveton, F. Novotny, M. Possolt, J. Prokupek, J. Proska, J. Psikal, L. Stolcova, A. Velyhan, M. Bougeard, P. D'Oliveira, O. Tcherbakoff, F. Reau, P. Martin, and A. Macchi, Phys. Rev. Lett. **111**, 185001 (2013).

[19] L. Fedeli, A. Sgattoni, G. Cantono, D. Garzella, F. Reau, I. Prencipe, M. Passoni, M. Raynaud, M. Kveton, J. Proska, A. Macchi, and T. Ceccotti, Phys. Rev. Lett. **116**, 015001 (2016).

[20] D. Zou, A. Pukhov, L. Yi, T. Y. H.B. Zhuo, Y. Yin, and F. Shao, Sci. Rep. **7**, 42666 (2017).

[21] D. Zou, D. Yu, M. Yu, T. Huang, A. Pukhov, H. Zhuo, C. Zhuo, and S. Ruan, Nucl. Fusion **59**, 066034 (2019).

[22] D. Zou, D. Yu, X. Jiang, M. Yu, Z. Chen, Z. Deng, T. Yu, Y. Yin, F. Shao, H. Zhuo, C. Zhuo, and S. Ruan, Phys. Plasmas **26**, 123105 (2019).

[23] L. A. Gizzi, D. Giove, C. Altana, F. Brandi, P. Cirrone, G. Cristoforetti, A. Fazzi, P. Ferrara, L. Fulgentini, P. Koester, L. Labate, G. Lanzalone, P. Londrillo, D. Mascali, A. Muoio, D. Palla, F. Schillaci, S. Sinigardi, S. Tudisco, and G. Turchetti, Appl. Sci. **7**, 984 (2017).

[24] L. L. Li, C. Y. Tsai, H. P. Wu, C. C. Chenb, and E. W. G. Diau, J. Mater. Chem. **20**, 2753 (2010).

[25] L. A. Gizzi, C. A. Altana, F. Brandi, P. Cirrone, G. Cristoforetti, A. Fazzi, P. Ferrara, L. Fulgentini, D. Giove, P. Koester, L. Labate, G. Lanzalone, P. Londrillo, D. Mascali, A. Muoio, D. Palla, F. Schillaci, S. Sinigardi, S. Tudisco, and G. Turchetti, Nucl. Instrum. Methods Phys. Res. Sec. A **829**, 144 (2016).

[26] L. Gizzi, F. Baffigi, F. Brandi, G. Bussolino, G. Cristoforetti, A. Fazzi, L. Fulgentini, D. Giove, P. Koester, L. Labate, G. Maero, D. Palla, M. Romé, and P. Tomassini, Nucl. Instrum. Methods Phys. Res., A **909**, 160 (2018).

[27] S. Keppler, A. Savert, J. Korner, M. Hornung, H. Liebetrau, J. Hein, and M.C. Kaluza, Laser Photon. Rev. **10**, 264 (2016).

[28] G. E. Kemp, A. Link, Y. Ping, H. S. McLean, P. K. Patel, R. R. Freeman, D. W. Schumacher, H. F. Tiedje, Y. Y. Tsui, R. Ramis, and R. Fedosejevs, Phys. Plasmas **22**, 013110 (2015).

[29] G. Cristoforetti, A. Anzalone, F. Baffigi, G. Bussolino, G. D'Arrigo, L. Fulgentini, A. Giulietti, P. Koester, L. Labate, S. Tudisco, and L. A. Gizzi, Plasma Phys. Control. Fusion **56**, 095001 (2014).

[30] C. Benedetti, A. Sgattoni, G. Turchetti, and P. Londrillo, IEEE Trans. Plasma Sci. **36**, 1790 (2008).

[31] H. Wei, D. Pan, and H. Xu, Nanoscale **7**, 19053 (2015).

[32] H. Wei, D. Pan, and H. Xu, Nano Lett. **11**, 471 (2011).

[33] A. Heron, J. C. Adam, and P. Mora, Phys. Plasmas **27**, 013103 (2020).

[34] M. Raynaud, A. Heron, and J. C. Adams, Sci. Rep. **10**, 13450 (2020).

[35] S. Segui, J. L. Gervasoni, and N. R. Arista, Radiat. Phys. Chem. **76**, 582 (2007).

[36] J. Kohl, M. Fireman, and D. M. O'Carroll, Phys. Rev. B **84**, 235118 (2011).

[37] J. Song, R. P. Zaccaria, G. Dong, E. D. Fabrizio, M. B. Yu, and G. Q. Lo, Opt. Express **19**, 25206 (2011).

[38] H. Ni, Y. Zhou, X. Liu, H. Ali, L. Ge, C. Pan, J. Chang, T. Wang, Q. Liu, and M. Wang, Opt. Mater. Express **8**, 3676 (2018).

[39] J. Babaei, L. A. Gizzi, P. Londrillo, S. Mirzanejad, T. Rovelli, S. Sinigardi, and G. Turchetti, Phys. Plasmas **24**, 043106 (2017).